First comparison of travelling atmospheric disturbances observed in the middle thermosphere by GOLD to travelling ionospheric disturbances seen in ground-based total electron content observations

Scott L. England[1], Katelynn R. Greer[2], Shun-Rong Zhang[3], Scott Evans[4], Stanley C. Solomon[5], Richard W. Eastes[2], William E. McClintock[2], Alan G. Burns[5]

[1] Aerospace and Ocean Engineering, Virginia Polytechnic Institute and State University, Blacksburg, Virginia, United States

[2] Laboratory for Atmospheric and Space Physics, University of Colorado Boulder, Boulder, Colorado, United States

[3] MIT Haystack Observatory, Westford, MA, United States

[4] Computational Physics, Inc., Springfield, Virginia, USA

[5] High Altitude Observatory, National Center for Atmospheric Research, Boulder, Colorado, United States

Corresponding author: Scott L. England (englands@vt.edu), Orcid: 0000-0001-5336-0040

Key points

1. Coordinated observations of atmospheric waves from GOLD and ionospheric TEC perturbations are presented
2. Perturbations consistent with a large-scale wave are seen moving horizontally at the same rate in both datasets

3. The amplitude and phase relationship between atmospheric and ionospheric parameters is not always clear

Abstract

Travelling ionospheric disturbances (TIDs) and their neutral counterparts known as travelling atmospheric disturbances (TADs) are believed to play a central role in redistributing energy and momentum in the upper atmosphere and communicating inputs to other locations in the fluid. While these two phenomena are believed to be connected, they may not have a one-to-one correspondence as the geomagnetic field influences the TID but has no direct impact on the TAD. The relative amplitudes of the perturbations seen in the ionosphere and atmosphere have been observed but rarely together. This study reports results from a three-day campaign to observe TIDs and TADs simultaneously over a broad latitudinal region over the eastern United States using a combination of GOLD and a distributed network of ground based Global Navigation Satellite System (GNSS) receivers. These results demonstrate that GOLD and the ground-based total electron content (TEC) observations can see the atmospheric and ionospheric portions of a large-scale travelling disturbance. The phase difference in the perturbations to the GOLD airglow brightness, O/N_2 and thermospheric disk temperature are consistent with an atmospheric gravity wave moving through this region. The ionospheric signatures move at the same rate as those in the atmosphere, but their amplitudes do not have a simple correspondence to the amplitude of the signal seen in the atmosphere. This campaign demonstrates a proof-of-concept that this combination of observations is able to provide information on TIDs and TADs, including quantifying their impact on the temperature and chemical composition of the upper atmosphere.

Plain Language Summary

Waves are a ubiquitous feature of the Earth's atmosphere. Just as with waves on the surface of water, these act to transport energy and momentum from the region in which they are produced to other parts of the fluid. A specific type of these waves in the upper atmosphere, often with spatial scales of hundreds to thousands of km, are known as travelling atmospheric disturbances (TADs). A signature that is often associated with these TADs is seen in the charged particle environment around the Earth, that are referred to as travelling ionospheric disturbances (TIDs). While it is widely accepted that TADs and TIDs are related, the exact relationship between their amplitudes and other quantities is not well established. This paper describes a campaign during which observations of the atmosphere (from NASA's GOLD mission) and charged particles (from ground-based observations) are combined in order to identify the relationship between the TAD and TID parameters. The GOLD observations of the upper atmospheric temperature, composition and its emissions are all consistent with what is known about TADs. At the same time, the ground-based observations of the charged particles reveal a TID that moves at the same speed as the TAD.

1. Introduction

Atmospheric gravity waves are believed to play a key role in redistributing energy and momentum within the Earth's atmosphere and communicating impacts in one region to physically distant locations. In the thermosphere, gravity waves are believed to be a key component of the wave spectrum that is present, and can significantly impact this region through dissipating momentum, generating mixing, local heating and flux of heat and minor constituents

(e.g. Yiğit & Medvedev, 2015). Many of the gravity waves seen in the thermosphere are believed to have propagated up from the lower atmosphere (as both primary and secondary waves, e.g. Vadas & Fritts, 2006; Vadas & Liu, 2009; Yiğit et al., 2014), while others are believed to have been generated at thermospheric altitudes through processes such as Joule heating in the auroral regions (e.g. Richmond, 1978) and the solar terminator (e.g. Galushko et al., 1998). During geomagnetic storms, particularly large amplitude gravity waves may be generated by impulsive heating of the atmosphere at high-latitudes (e.g. Shiokawa *et al*., 2007).

Atmospheric gravity waves are often described alongside their ionospheric counterparts, where the former is referred to as travelling atmospheric disturbance (TAD) and the latter as a travelling ionospheric disturbance (TID). TIDs are typically grouped into two categories according to their horizontal wavelengths / spatial sizes. Large-scale TIDs are typically classified as having wavelengths over 1,000 km. Large-scale TIDs are often believed to be accompanied by TADs generated in the auroral regions (e.g. Bruinsma et al., 2006). Medium-scale TIDs are typically classified as having horizontal wavelengths in the 100 – 1,000 km range. These medium-scale TIDs are believed to often be accompanied by TADs generated in the lower regions of the atmosphere (e.g., Azeem et al., 2017), while others are not (especially at mid-latitude during the night).

Surveys of both atmospheric and ionospheric observations have revealed that TIDs/TADs are present under almost all conditions, at some amplitude. At the mid-latitudes that will be considered in this study, results such as Livneh *et al*., [2009] have revealed TID-like fluctuations in the ionosphere that are omnipresent, with periods in the 30 – 60-minute range. Tsugawa *et al*.,

[2007] presented an analysis of ground-based total electron content (TEC) variations, showing abundant waves with horizontal wavelengths in the 300 – 1000 km range over North America, consistent with medium-scale TIDs. Recently, Tsuchiya *et al*., [2020] used 10 years of ground-based observations from a variety of sites and found a variation in the horizontal wavenumber spectrum observed with location. Mandal and Pallamraju (2020) also identified that the vertical propagation of gravity waves in the thermosphere varies with season at low-latitudes, which may impact the ability of some waves originating the lower atmosphere to form TAD and TID perturbations.

Direct observations of TADs are relatively rare, compared to the broad survey ionospheric data such as ground-based TEC that have permitted extensive studies of TIDs. *In situ* atmospheric observations of TADs are most commonly available in the upper thermosphere where sustained spaceflight is possible (e.g., Bruinsma & Forbes, 2008; Garcia *et al*., 2016; Park *et al*., 2014). A large fraction of the observations at altitudes below these orbital altitudes come from observations of TIDs, from which the existence and properties of a TAD are inferred (e.g. Djuth *et al*., 2010; Galushko *et al*., 1998). Negrea *et al*., [2016] used an extensive ionospheric dataset and established that the TID characteristics seen were consistent with the theoretical properties of acoustic gravity waves. Concurrent ion and neutral observations of waves have been made *in situ* (e.g., Earle *et al*., 2008; Paulino *et al*., 2018) which have demonstrated that the TIDs are often a good proxy for the TAD. Given that TID observations are readily available and that they are often used to infer the TAD, further study of the relationship between these two using simultaneous observations is of importance and will be the focus of this study.

NASA's Global-scale Observations of the Limb and Disk (GOLD) mission of opportunity provides measurements of the middle thermosphere over the daylit disk of the Earth visible from geostationary orbit over the Amazon river delta (Eastes *et al*., 2017). It has been demonstrated that by using a dedicated campaign mode, GOLD is able to observe TADs as they move through this region (England *et al*., 2020). This provides thermospheric measurements over a latitudinally broad region which, when combined with distributed ground-based ionospheric observations, offers an opportunity to examine the relationship between TIDs and TADs over low to mid-latitudes. England *et al*., [2020] presented results of an extremely limited (6 hour) campaign that took place during the commissioning phase of the GOLD instrument. The selection of the viewing location on the disk meant that virtually no ground-based data were available during this campaign. Here we report results of a follow-on campaign that built upon lessons learned and focused on establishing how well we can compare the TADs observed by GOLD to TIDs seen in ground-based TEC observations. Key changes to the campaign setup will be described in more detail in the next section, but include: 1) extending the duration from one to three days; 2) providing overlap with ground sites; 3) identification of perturbations to both the N_2 airglow and the temperature of the middle thermosphere, which provide substantially more data with which to characterize the waves present.

2. Experimental Setup and Data Used

This section will discuss the observational campaign performed by GOLD, and its associated data; the geophysical conditions present during the campaign; and the ground-based TEC data used to provide larger-scale context and daytime ionospheric parameters.

2.1 Experimental setup

GOLD is a 2-channel far-ultraviolet (FUV) imaging spectrometer that observes the Earth from onboard the SES-14 geostationary communications satellite, which is located at -47.5° longitude (Eastes *et al*., 2017; McClintock *et al*., 2017; Eastes *et al*., 2019). During regular operations, when GOLD's Field of View (FOV) is illuminated by the sun, the instrument scans the disk of the Earth, building up an image of the Earth's full disk with a 30-minute cadence. GOLD makes observations between ~134 and 167 nm, which allows identification of the prominent dayglow features of O at 135.6 nm and LBH bands of N_2. While the ratio of the brightness of these two features conveys information related to the composition of the thermosphere (column O/N_2 ratio), the shape of the N_2 LBH emission bands can be used to determine the temperature of the thermosphere. During October 2019, Channel B of the GOLD instrument was used to perform a special mode campaign, designed to identify the impacts of atmospheric waves on the middle thermosphere and their relation to similar fluctuations in the ionosphere. This basic experimental setup follows that described in England *et al*. [2020], but with several important changes. The prior campaign demonstrated that GOLD is able to detect wave-like signatures in the airglow when it changes from regular operations in which it scans the Earth's disk, and instead stares at one location (one near vertical line as shown in Figure 1) for several hours. This staring has the effect of increasing the signal by a factor of over 100 times compared to the scanning mode while sacrificing the instrument's ability to continue regular data collection. To both meet this need for a non-scanning mode, and not interrupt the regular GOLD data collection, a single channel of the instrument (Channel B) was used for this campaign. As regular operations were not interrupted, this enabled a longer campaign, spanning 3 consecutive days (October 17 – 19th, 2019), with campaign data taken with Channel B from 12:30 – 20:00 hours UTC. In the initial

campaign described by England *et al*. [2020], the availability of both GOLD channels allowed for the identification of the wave propagation direction, velocity and wavelength. With only a single channel, this is not possible. To both meet this need and provide information on any ionospheric perturbations that were not available during the initial campaign, concurrent data from ground-based observatories was considered when designing this campaign. By positioning the Channel B slit off-nadir, centered on the United States East Coast region, many sites observing TEC using GNSS radio signals are available and fill both needs described above. Figure 1 shows the location of the observations from Channel B that will be the focus of this study. All of these are Level 2, version 2 GOLD data (available from https://gold.cs.ucf.edu).

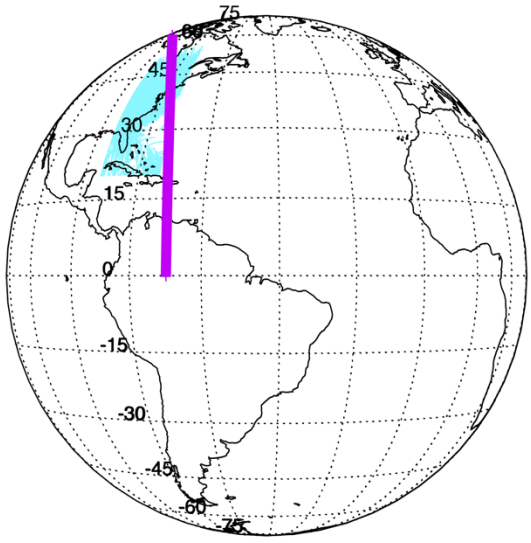

Figure 1 Location of the GOLD Channel B observations during the campaign. A purple plus symbol marks the location of each of the 376 data bins along the length of the image. The light blue dots show the locations of the GPS dTEC data included in this study.

2.2 GOLD Airglow Brightness

To determine the fluctuations in the airglow brightness, this study uses the Level 1b (L1b) data from the GOLD instrument, which are described in the Data Products Users Guide (see https://gold.cs.ucf.edu). The L1b files are available for this campaign at 2-minute cadence and provide the spectra in instrument counts vs wavelength and latitude. The L1b processing includes geometric corrections for the detector and optics, filtering of the counts based on the detector pulse heights, a correction based on the detector deadtime (maximum count rate) and data are binned on a regular wavelength scale. England *et al*., [2020] also used the Level 1c data, which provide the calibrated brightness in Rayleighs, but at both a lower temporal cadence (10 minutes) and much lower spatial resolution (125 x 125 km^2). From that prior study, it is evident that the perturbations to the airglow are relatively small in amplitude (below 1%) and are more easily seen in the L1b data that we will use here.

2.3 GOLD Disk Temperatures

GOLD makes measurements of the thermospheric temperature by observing the shape of the N_2 LBH bands in the ~137 – 160 nm wavelength range (see Eastes *et al*., 2017). This technique was first demonstrated by Aksnes *et al*., [2006] using limb observations from the High-resolution Ionospheric and Thermospheric Spectrograph (HITS) on the Advanced Research and Global Observation Satellite (ARGOS). The LBH emission provides information on the neutral temperatures in the middle thermosphere, with the maximum weighting to an altitude around 160 km (i.e. near the altitude of peak emission). Here we consider these disk temperature data, which are Level 2 products. For the disk scanning mode (e.g. Figure 1) these are available at a 30 minute cadence, but for Channel B these are available at a 10 minute cadence, with a resolution corresponding to 40 spatial pixels along the slit for which temperature can be derived (emission

198 angle constraints prevent determining temperatures very close to the limb as seen in Figure 1b).
199 At the higher count rate per spatial-temporal bin that is obtained during the special mode
200 campaign, the average random uncertainty per bin is 9.4 K (discussed further in Section 3.3)
201
202
203 **2.4 GOLD Column O/N_2 Ratios**
204 GOLD makes measurements of the thermospheric column O/N_2 ratio by observing the ratio of
205 the brightness of the 135.6 nm O doublet to the brightness of the N_2 LBH band in the ~137 – 160
206 nm wavelength range (see Eastes *et al*., 2017). Use of disk observations of these emissions to
207 determine the thermospheric column O/N_2 ratio was first demonstrated by Strickland *et al*.,
208 [1995] and has been widely used with data such as from TIMED-GUVI (e.g. Zhang *et al*., 2004).
209 The O/N_2 ratio is indicative of the ratio of the column density of these two species from infinity
210 down to an altitude corresponding to an N_2 column density of 10^{17} cm^{-2}, which is typically
211 around 140 km. Here we use the GOLD Level 2 O/N_2 data. These are available at the same
212 resolution and cadence as the disk temperatures described above.
213
214 **2.5 Differential TEC**
215 Ground-based estimates of TEC from GNSS radio signals are routinely produced using
216 algorithms developed at MIT Haystack Observatory (Rideout and Coster, 2006; Vierinen *et al*.,
217 2016). Previous studies have used these data to identify travelling ionospheric disturbances,
218 which have revealed that this is most easily detected in differential TEC (dTEC) values, rather
219 than the absolute TEC values (e.g., Zhang *et al*., 2019). Following the methodology in Zhang *et*
220 *al*., [2019], we adopt a cut-off elevation angle of 30°, below which ground-satellite ray paths are

excluded. Differential TEC values are computed by first removing the background TEC using a low-pass Savitzky-Golay filter (Savitzky and Golay, 1964). This de-trending analysis is applied to each of the TEC data segments of individual line-of-sight measurements between a GNSS satellite and a receiver. Examples of these data are shown in Figure 2 as functions of time and latitude at three different longitudes around the GOLD observations. The GOLD slit near 40° north is around 77° west.

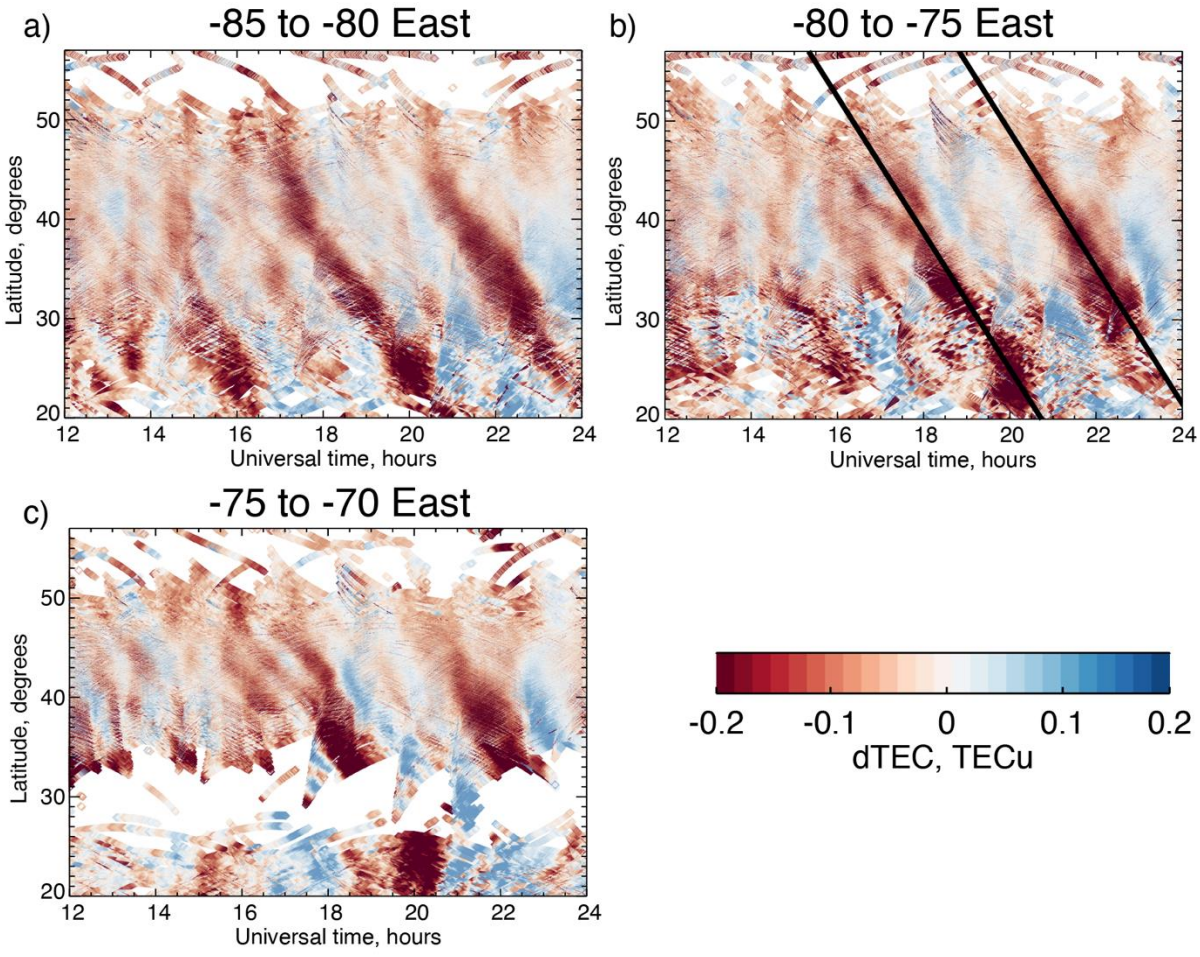

Figure 2 Global Navigation Satellite System differential TEC (dTEC) for October 18, 2019 as functions of latitude and universal time. The range of longitudes included is indicated in panels a

through c. The overlaid black lines in panel b mark locations of local maxima used to find the approximate latitudinal phase velocity of the features seen, as described in the text.

2.6 Geophysical Conditions

The F10.7 index (available from NASA's OMNIWeb at https://omniweb.gsfc.nasa.gov) is between 64 and 66 throughout the three days of the special mode campaign, representing extremely low and steady solar EUV flux values. Of more note is the impact that any heating of the thermosphere associated with the auroral electrojet may have, as this is believed to be a major source of TADs (e.g. Shiokawa *et al.*, 2007). Figure 3 shows the 1-minute SME auroral electrojet index from SuperMAG (Newell and Gjerloev, 2011; Gjerloev, 2012) for October 17th through 19th, 2019. The overall SME index is moderate throughout, but it is worth noting that there is a slightly elevated electrojet on the third day, both before and during the hours of the daytime thermospheric observations.

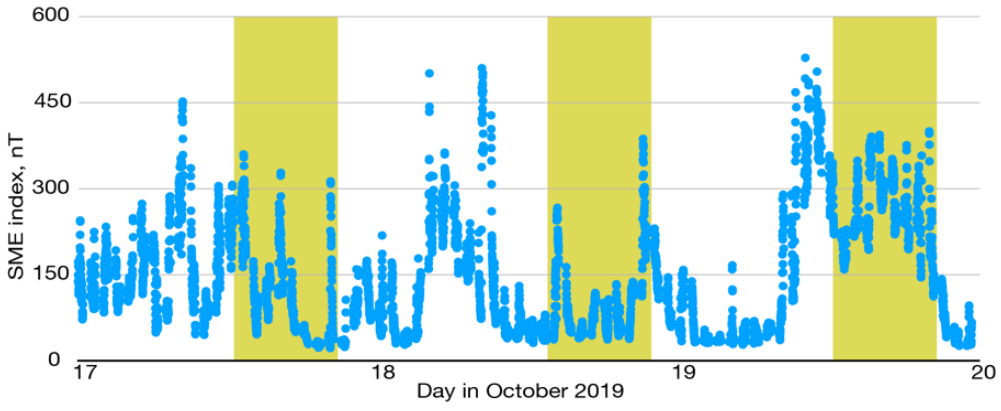

Figure 3 One-minute SME Auroral Electrojet Index for the 3 days of the campaign during October 2019. The time-periods corresponding to the GOLD observations are highlighted with the yellow shaded regions.

3. Method and Results

This section describes the analysis of each dataset, starting with the differential TEC which is used to guide the analysis of the GOLD airglow and temperature data. The middle day of the campaign (October 18th, 2019) will be shown throughout to demonstrate the methodology, and results from all three days, combining all three datasets are shown in Figure 6.

3.1 Differential TEC

Given the elevation angle constraint described in Section 2.4, the dTEC data are confined to the land and coastal regions. As seen in Figure 1, the GOLD observations cross over the land and ocean. The greatest overlap in the available data between the TEC and GOLD observations occurs over the east coast of the United States, corresponding to the latitude range of 75 – 80° west shown in panel b of Figure 2. This region overlaps the GOLD FOV well from around 35 - 50° north. Further north, there is very little dTEC data available, and further south the GOLD FOV lies further to the east (see Figure 1). Hence, we will focus primarily on the variations seen in this latitude band at this time.

As noted in previous studies, the dTEC observations often reveal wave-like oscillations associated with TIDs. Many of these are evident in Figure 2, with different propagation directions and periods. Focusing on the latitude region from 35 – 50° north, clear features are seen near 18- and 22-hours UT moving in a southward direction in all 3 panels (highlighted in panel b), with a third feature around 14 hours UT visible in panels a and b. As these features are clear in all 3 panels and appear to be the strongest observed, we will focus on these. Using the

data shown in all 3 panels, it is possible to estimate the phase speed of the TID seen. This is done in four steps. 1) Points close to the positive phases of the wave are identified by eye, and these are used as initial inputs. 2) Data for 1 hour around each location are then chosen. 3) A cubic-spline interpolation to these values is used to provide data at regular spacing and the local maxima is identified. 4) The results of step 3 are compared to the location of the maximum value in the data from step 2 to ensure the results of step 3 are not numerical artifacts. A least-squares linear fit to these is used to determine an estimate of the latitudinal phase velocity of this TID at ~7°/hour (shown with the solid black lines in panel b).

Leveraging the other available dTEC data in panels a and c, it is possible to identify the horizontal wavelength and phase velocity of the observed TID. This is done by using the observations from the 3 longitudes shown, and assuming that the wave has plane wavefronts. The phase difference between the 3 longitudes provides information on the azimuth of the wave phase velocity. In this case we see no appreciable difference, indicating the wave propagation direction is nearly due south. With this, and estimating the dTEC observations to be coming from around 300 km altitude and above, 7 degrees/hour corresponds to a phase speed of ~210 m/s. The wavelength estimated in this way are within the range of large-scale TIDs reported previously (see Section 1), although it is worth noting that the phase velocity identified is slow compared to many larger-scale TIDs reported. The wave speed and heading are indicative of a wave source in the auroral region, but a lower-atmospheric source or secondary gravity wave remain other plausible possibilities.

Clearly other wave features are seen in Figure 2. A full analysis of all of these is beyond the scope of this study. Instead, we will focus on this clearest wave feature and investigate if a corresponding signature in the atmosphere is observed simultaneously by GOLD. This will be done in-part by using the propagation rate determined from the dTEC observations and comparing this to that seen in the GOLD observations. This process will tend to identify the features shown in panel b of Figure 2, and minimize any other wave features present.

3.2 GOLD Airglow Radiances

GOLD is able to see perturbations to the FUV airglow caused by atmospheric waves in the middle thermosphere. To identify these perturbations, we follow the method of England *et al*., [2020], but here extend it to include the N_2 LBH bands, in addition to the OI 135.6 nm doublet. This is done in three steps. Step 1) Identify these two emission features and subtract any background emission. Wavelength bins within the GOLD spectrum that correspond to the 135.6 nm doublet and the nitrogen band (including the atomic nitrogen line at 149.3 nm that responds in a similar manner to the LBH bands; Zhang *et al*., 2018) are identified. These are highlighted in Figure 4 by the light blue and yellow symbols. The brightness in each of these (measured in Level 1b counts) is summed up at each spatial pixel and each point in time. To determine the background level, wavelength ranges adjacent to these are used. These are highlighted in Figure 4 by the dark blue and purple symbols. The brightness in each of these is summed up and the value subtracted from the in-band emissions found above (after normalizing for the number of spectral bins). Step 2) Identify and remove the strong local-time variation associated with solar zenith angle (note that the emission angle is constant for each pixel during this campaign). This is done by fitting a third-order polynomial to the time-series of data for the two emissions

identified above at each spatial pixel. The brightness variations associated with this low-order fit are then removed. Step 3) Identify and remove any change in brightness that occurs at all points along the disk simultaneously that are associated with small changes in solar EUV flux during the day. The mean value of the brightness across the pixels on the image is found and removed from the detrended data. The output of steps 2 and 3 is a residual signal with a mean value of zero. Following England *et al*., [2020], we then reduce the extremely noisy 2-minute L1b residual data with a 10-minute rolling median filter on the time-series at each spatial pixel. This removes outlying high and low data points, while preserving a much higher temporal cadence than the oscillations seen in the dTEC values in Figure 2 and **Error! Reference source not found.**.

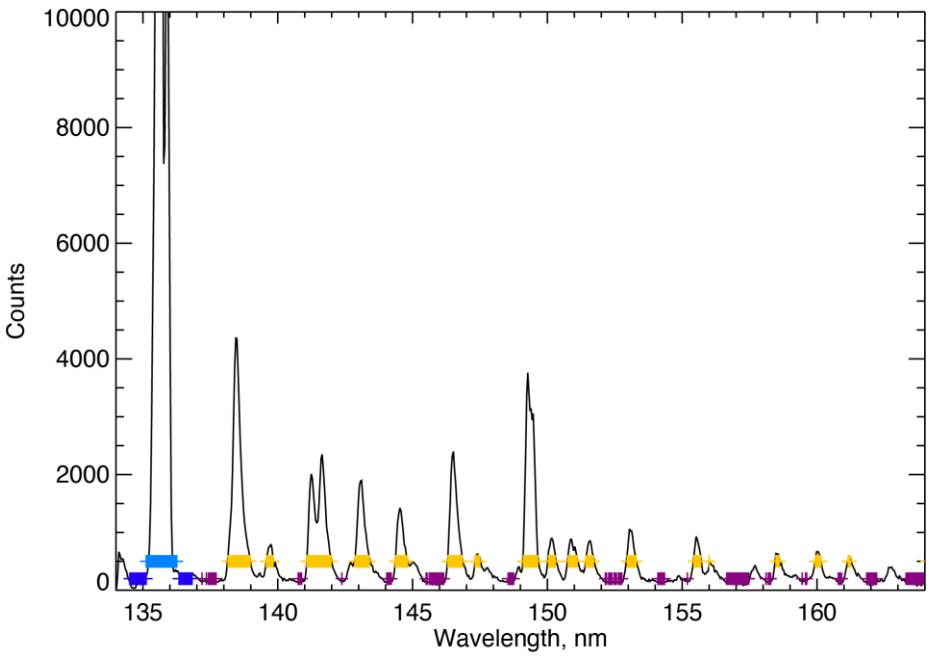

Figure 4 Example spectrum made from summing 100 Level 1b exposures from the GOLD data from October 18, 2019. The light blue symbols highlight the region used to identify the atomic oxygen feature and the dark blue highlight the corresponding background area. The yellow

symbols highlight the region used to identify the nitrogen features and the dark purple highlight the corresponding background area.

Figure 5 panels a and b show the detrended L1b values for the oxygen and nitrogen emissions, respectively. The large variations in brightness seen at the very northernmost extent of the GOLD data, above ~60° latitude could be associated with variations in the aurora that lies close to the edge of the FOV, and therefore we will focus on the region equatorward of this. Similar to the dTEC perturbations seen in Figure 2, fluctuations in the brightness in both oxygen and nitrogen emissions are seen, which appear to move southwards with time. The amplitude of these fluctuations is small compared to the mean brightness. In the case of the oxygen airglow, the mean brightness on this day is 643 counts, whereas the fluctuations are ~10 counts, or ~0.4% of the mean. This small amplitude is consistent with that reported by England *et al*., [2020]. It is worth noting that the latitudes for which dTEC observations are available lie well away from the equatorial anomaly, which avoids any impact this may have on either these or the 135.6 nm airglow.

Given the low amplitude of the features observed, it is worthwhile determining the detection limit of the GOLD instrument in this mode. Assuming that the 135.6 nm signal is dominated by Poisson noise, 643 counts would give a per pixel signal-to-noise ratio of 25.4. Thus, a signal of level 3.9 % would have a signal-to-noise ratio (SNR) of 1. To identify a signal as small as 0.4 % with an SNR of 1, such a feature would need to be present in approximately 100 pixels. The data shown in Figure 5 span 350 pixels in space and the wave-like features appear to fill the entire observable latitude range, allowing for unambiguous determination of these features, despite the

low amplitude signal. This will be especially important when considering the data in Figure 6, where these data have been reduced to a single line-plot.

Comparing the variations in the oxygen airglow with those in the nitrogen, these fluctuations appear to be out of phase with one another such that an increase in the brightness of the oxygen airglow is approximately correspondent with a decrease in the brightness of the nitrogen airglow. This is consistent with the effect of vertical advection, which tends to increase (decrease) oxygen relative to nitrogen when such advection is downwards (upwards). To investigate this in a more quantitative manner, Figure 5 panel c shows the difference in the oxygen airglow and the nitrogen airglow. As the amplitude of the fluctuation in the nitrogen appears lower everywhere below the aurora, we multiply it by two and then subtract it from the oxygen perturbation. This signature of the oxygen – nitrogen difference appears almost exactly in phase with the oxygen airglow, confirming the out-of-phase relationship of the emissions from the two species.

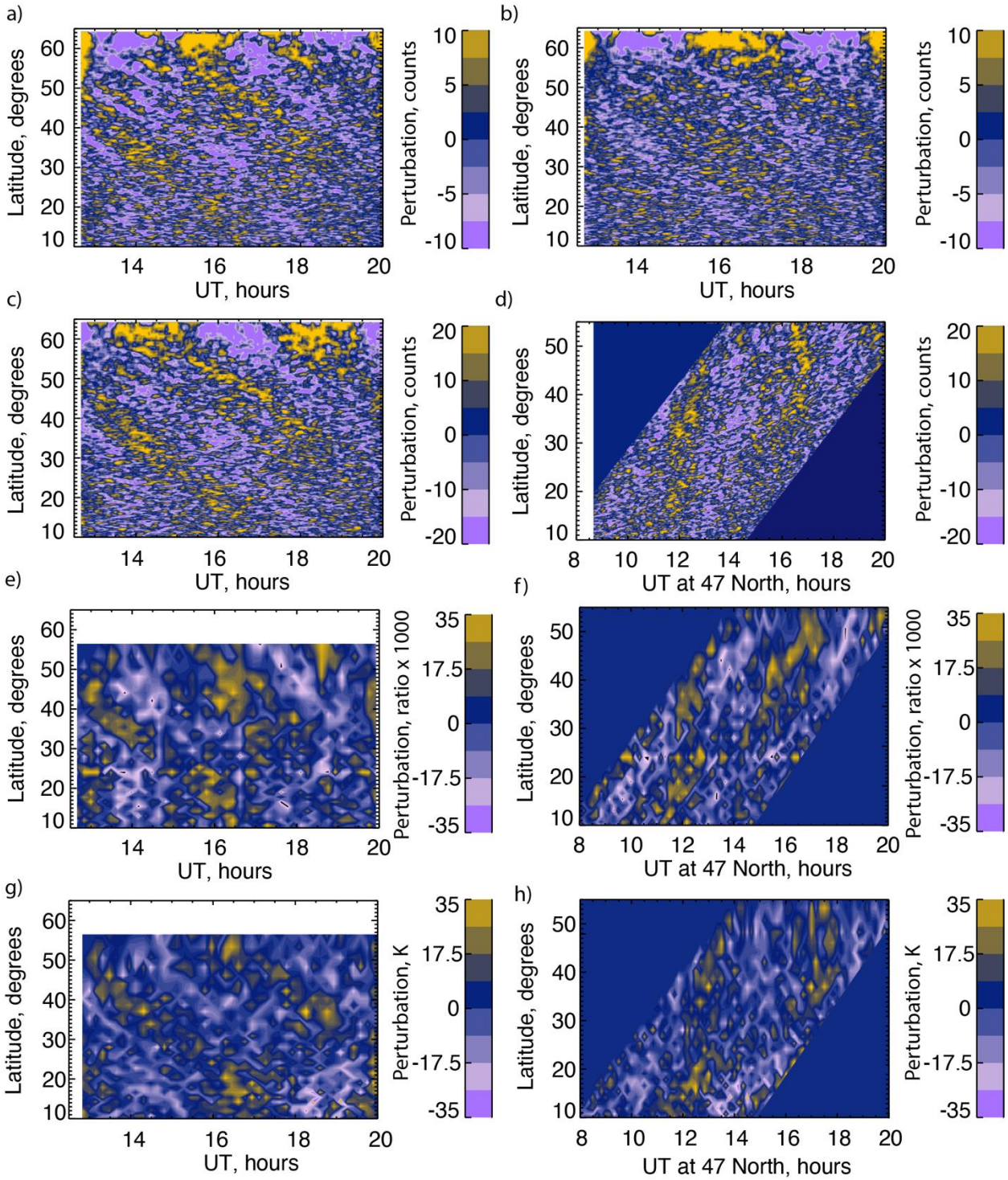

Figure 5 Perturbations to the airglow, composition and temperature observed on October 18, 2019. Panel a shows the perturbation in the oxygen airglow. Panel b shows the perturbation in the nitrogen airglow. Panel c shows the perturbation in the oxygen minus twice the nitrogen

airglow to highlight the difference. Panel d shows the oxygen airglow minus twice the nitrogen airglow, where the universal times at each latitude have been offset to correspond to the time at 47° latitude, using the latitudinal phase propagation rates derived from the dTEC data, as described in the text. Panels e and f are as c and d, but for the column O/N_2 perturbations derived from the oxygen and nitrogen airglow brightnesses. Panels f and h are as c and d, but for the perturbations in the disk temperature derived from the shape of the LBH band emission.

Visually comparing to Figure 2 it is not immediately clear if these are the very same fluctuations as seen in dTEC or not. To investigate this further, we can establish if the perturbations are moving at the same rate as those shown in Figure 2. This is done by shifting the GOLD data at each latitude back to a reference at 47°, using the phase propagation rate found from the dTEC data. The choice of 47° latitude is arbitrary, and simply falls within the range of good overlap between GOLD and the dTEC values – the use of any other latitude would simply shift the epoch for the horizontal axis. If the perturbations seen by GOLD are moving at the same rate as those seen in the dTEC data, the result should show perturbations that appear vertical in this latitude – modified universal time coordinate system. This is shown for the oxygen – nitrogen differences in Figure 5 panel d. While the perturbations are not perfectly vertical in this figure, it is clear that the airglow perturbations are moving in latitude at the same rate as those seen in dTEC, supporting the hypothesis that the two datasets are seeing related features in the atmosphere and ionosphere, respectively. The correspondence between each dataset in this shifted coordinate system is explored in more detail in Section 3.5.

3.3 GOLD Disk Temperatures

Having established that GOLD observes fluctuations in the brightness of the airglow that appear to move with those seen in the TEC data, we now consider the GOLD observations of the temperature of the middle thermosphere. As described in Section 2.3, these are available over a slightly reduced region relative to the airglow brightness data, but still cover all of the latitudes seen in the TEC data. As with the airglow brightness the temperature exhibits a strong local time dependence, and so the same detrending procedure as described in Steps 2 and 3 in Section 3.2 is applied to the temperature data. The resulting detrended temperatures are shown in Figure 5 panel g. It is clear that similar perturbations are seen in the temperatures as the airglow brightness, but with some shift in the phase of the signature (approximately one quarter wavelength). For the disk temperature data included in Figure 5, the average random uncertainty per spatial-temporal bin is 9.4 K. The temperature perturbation seen appears to be around twice this value, and also is present across many bins at once, yielding a relatively unambiguous determination of this moving feature. Following the analysis described above, Figure 5 panel h shows the temperature data that have been shifted using the rate from the dTEC data. This again supports the hypothesis that the perturbation seen by GOLD is related to that seen in the dTEC data.

3.4 GOLD Column O/N_2

Given the variations seen in the oxygen and nitrogen airglow features described in Section 3.2, it is expected that measurable changes in the column O/N_2 will be present during this campaign. Using the Level 2 GOLD data provides an opportunity to determine the amplitude of this variation and compare this to the signatures identified in the temperature and ionospheric observations. As with the airglow brightness the O/N_2 exhibits a strong local time dependence,

and so the same detrending procedure as described in Steps 2 and 3 in Section 3.2 is applied to the O/N_2 data. The resulting detrended column O/N_2 are shown in Figure 5 panel e. These follow a similar pattern to those in panels c and d that show the differences in the brightnesses of the oxygen and nitrogen airglow, as may be expected.

When interpreting such small changes in column O/N_2 derived from Far UV observations, it is important to acknowledge that the 135.6 nm observations used to determine O/N_2 contain a small contribution from O^+ radiative recombination, in addition to the photoelectron impact on O. Using the dTEC observations, we can estimate the impact this may have, relative to the O/N_2 perturbations reported here. First, we select a location corresponding to approximately the middle of where the perturbations are seen (40° north, 77° east and 15 hours UT). At this location, we use an ionospheric O^+ density and electron temperature profile from IRI-2016 (Bilitza, 2018) and the radiative recombination airglow coefficients from Melèndez-Alvira et al. (1999) to estimate the total emission from O^+ radiative recombination in this region to be ~19 R, compared to the mean GOLD observed value of 1000 R. From the magnitude of the perturbation seen in TEC, we can estimate that this O^+ radiation recombination may vary by 1.7 R, or 0.17% of the mean brightness. Comparing this to the observed variation in 135.6 (Section 3.2), which is around 0.4 % of the mean, we see that this radiative recombination may account for a little less than half of the total signal. This is consistent with a comparison of the signatures seen in the dTEC and 135.6 nm observations, which appear similar but not identical as the 135.6 nm signature is a mixture of the O and O^+ perturbations.

3.5 Correspondence between observed parameters

For a more quantitative comparison of the three datasets, we make use of the UT shift shown in Figure 5 to align all of the major perturbations such that they occur at all latitudes at approxiomately the same shifted UT. This then allows us to average the signal over a range of latitudes, which compensates for the relatively low magnitude of the perturbation in the airglow brightness data. In effect, this emphasizes only the features moving at the rate of those shown in Figure 2, but as described in Section 3.2, it increases the signal-to-noise ratio for those signatures. A latitude range of 20 – 50° is chosen as the perturbations are clear throughout this region, and all datasets have good coverage throughout this latitude range. Figure 6 shows the results of this for all three days of the campaign.

Examining Figure 6 panels a, e and i, a clear antiphase relationship is seen between the oxygen and nitrogen airglow. This is further verified by examining Figure 6 panels b, f and j, which show that the perturbations in the retrieved column O/N_2 look extremely similar to the variations in the oxygen airglow brightness. This signature is a clear sign of vertical advection, which in combination with the different altitude distributions of oxygen and nitrogen in the middle thermosphere, acts to increase the column abundance of one of these relative to the other. The oscillatory nature of the signatures would also be consistent with this advection being caused by anatmospheric wave moving through this region.

Examining Figure 6 panels c, g and k we see the relationship between the oxygen ariglow and temperature perturbations. While not perfect, a clear relationship between the two is apparent. Rather than a simple in phase or out- of phase relationship, the positive and negative perturbations in the temperature appear to lag those seen in the oxygen airglow brightness by

approximately one quarter of the wave period. This phase relationship is consistent with an atmospheric gravity wave propagating southwards with time, where we may expect to see the increase in atomic oxygen that is associated with downward advection one quarter wave period before the increased temperatures (e.g. Andrews *et al*., 1987).

Examining Figure 6 panels d, h and l the relationship between the perturbations in the oxygen airglow brightness and dTEC is less clear. Nontheless, some features appear in common, especially on the first two days of the campaign. On these two days, the increases in dTEC and oxygen airglow brightness appear to be roughly in phase, although the amplitudes of the perturbations do not appear to have a simple correspondence such that sometimes a large increase in airglow is seen at the same time as a small increase in dTEC, and vice versa. It is also worth noting that the rate of motion of the signatures seen in dTEC, airglow brightness, column O/N_2 and disk temperatures are all approximately the same (the rate of motion in dTEC is used to detrend all datasets into the shifted UT frame used here).

The following section will explore the consistency between the magnitude of the neutral atmosphere feature seen with our understanding of the oxygen airglow. For this, we note from Figure 6 the typical magnitudes seen in these parameters. From Figure 6 panels a, e and i we see a typical amplitude of the oxygen airglow brightness of 2.5 counts, compared to a mean value of 640 counts, which corresponds to ~0.4 %. From panels c, g and k we see a typical disk temperature amplitude of 13 K (compared to a mean temperature of 710 K). The correspondence of these will be examined in the next section.

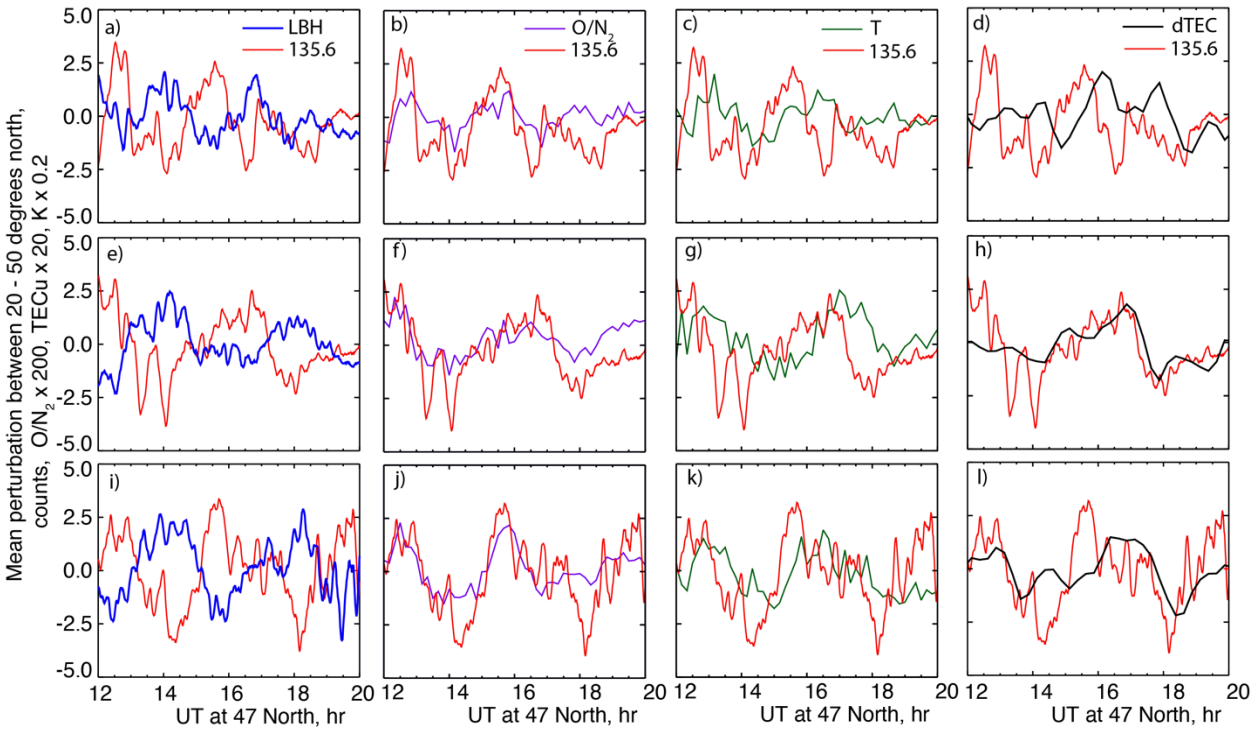

Figure 6 Panels a through d show the mean perturbation in the 135.6 nm airglow compared to the LBH airglow, column O/N_2, disk temperatures, and dTEC perturbations respectively. All data are averaged over 20 – 50° latitude, and are shifted in UT to a common value at 47° north as in Figure 5. Panels a through d correspond to the results for October 17, 2019. Panels e through h show the same as a through d, but for October 18, 2019. Panels i through l show the same as a through d, but for October 19, 2019. In each panel, the red line corresponds to the oxygen airglow. The airglow values are in counts. The disk temperatures are in K and are multipled by 0.2 to be visible on this scale. The column O/N_2 are dimensionless ratios and are multipled by 200 to be visible on this scale. The dTEC values are in TECu and are multiplied by 20 to be visible on this scale.

For a more quantitative assessment of the correspondence between the various parameters shown in Figure 6, we examine the relationship between sets of these parameters. This is done in the

following steps: 1) interpolate all quantities onto a common 10-minute temporal cadence (to match the lowest cadence) using a cubic-spline interpolation; 2) shift the temperature data by 1 hour, corresponding to the apparent one-quarter wave period shift seen in Figure 6; 3) plot corresponding pairs of data in the scatterplots shown in Figure 7; 4) as all perturbations are extremely small we can expect an approximately linear relationship between different quantities, which is found with a least-squares fit to the data in Figure 7 (shown by the pink solid lines); 5) compute the coefficient of determination (R^2) value for each set of parameters shown.

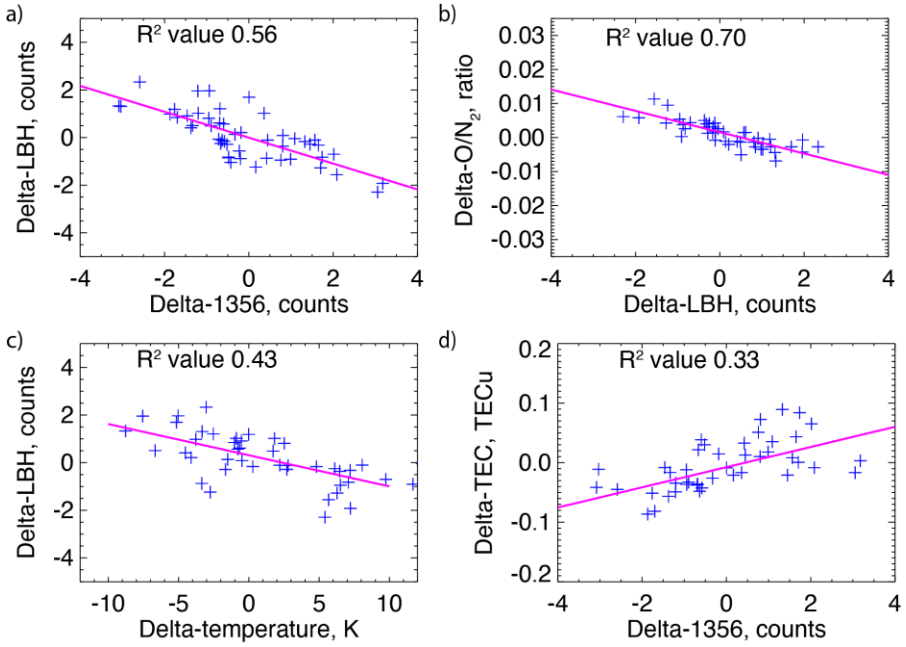

Figure 7 Correlations between the perturbations in the oxygen and nitrogren airglow brightness, disk temperatures, column O/N_2 and dTEC for October 18 2019 data shown in Figure 6. Panel a shows the nitrogen airglow brightness vs the oxygen airglow brightness. Panel b shows the O/N_2 ratio vs the nitrogen airglow brightness. Panel c shows the nitrogen airglow brightness vs the disk temperature. Panel d shows the dTEC vs the oxygen airglow brightness. All datasets have been interpolated onto a 10-minute cadence, and the temperature data were shifted by 1 hour,

corresponding to approximately one quarter wave period. The pink lines show the least-squares linear fits to each pair of data. Coefficients of determination for each of these linear fits are shown.

Examining panel a of Figure 7, we see the near anti-phase relationship between the oxygen and nitrogen airglow brightness perturbations that is expected from the earlier results. The best-fit linear trend shows a reasonable, but certainly not perfect agreement with the data, with a coefficient of determination of 0.56. Given this, it is worth considering how closely we may expect the fit to be to the data. From Section 3.2, we can tell that a signal with the apparent amplitude of that observed would have a SNR per 10-minute bin of approximately 3 for the oxygen airglow and approximately 2 for the nitrogen airglow. Also, it is worth noting that these estimates assume the signal is present across the entire latitude range selected (which appears to be the case based on Figure 5), and that the features moving at the rate determined from the dTEC perturbations characterize the only airglow perturbations present. This latter condition is likely not the case, based on Figure 2. With these two factors taken into consideration an R^2 value of no more than about 0.56 may be expected.

Examining panel b of Figure 7, we see the expected good anticorrelation between the column O/N_2 ratio and the nitrogen airglow brightness. The higher R^2 value of 0.7 suggests that any impact of O^+ radiative recombination in the determination of column O/N_2 perturbations does not have a significant impact on the pattern of O/N_2 perturbations that are found.

Examining panel c of Figure 7, we see some anticorrelation between the nitrogen airglow and the time-shifted disk temperature perturbations. While the R^2 value of 0.43 reflects a somewhat poor fit, no correspondence between these parameters is seen with the 1-hour time shift in the temperature data (R^2 value of $4x10^{-5}$ in this case). This confirms that the apparent one-quarter period shift expected by theory and seen in Figure 6 is a reasonable fit to the data.

Finally, examining panel d of Figure 7, we see some positive correlation between the oxygen airglow and the dTEC perturbations. The low R^2 value of 0.33 reflects what was noted in regard to Figure 6, that the perturbations in the ionosphere do not simply look like those in the neutral atmosphere, although they are apparently moving southwards at the same rate.

3.6 GLOW Model Results

Following England *et al*., [2020] it is possible to use the magnitude of the oxygen airglow brightness perturbation to estimate the amplitude of the underlying atmospheric perturbation. With the addition of the disk temperature data included in this study, we can also establish how consistent the estimated atmospheric perturbation is with the variation in the brightness of the airglow seen. Following Greer *et al*., [2018], we use the thermosphere-ionosphere-electrodynamics GCM (TIEGCM v2.0; Maute, 2017) model to provide information on the background atmosphere, onto which sinusoidal perturbations are applied that modify the atmospheric density and temperature in the middle thermosphere, as described in Section 2 of Greer *et al*., [2018]. We then use the Global Airglow model (GLOW; Solomon, 2017) to simulate the 135.6 nm O airglow GOLD would observe at 45° north and 80° west, for the given geophysical and solar conditions corresponding to October 18, 2019. By varying the amplitude

of the induced perturbation, we can find the amplitude of a wave in the middle thermosphere that would produce a perturbation in the airglow of the same amplitude as observed by GOLD.

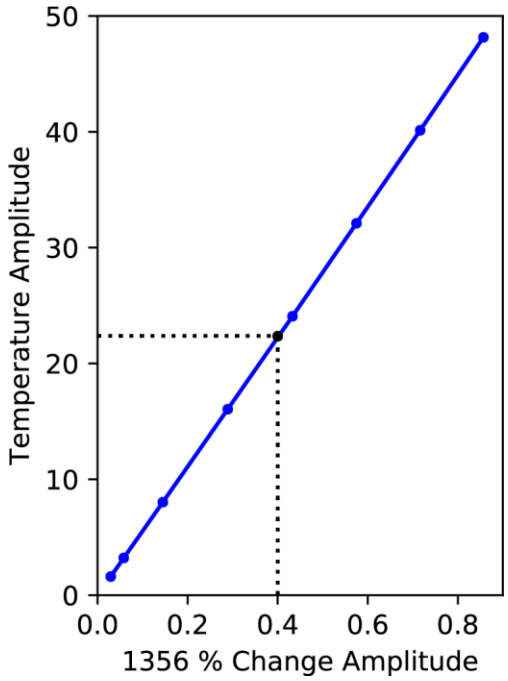

Figure *8* shows the results of these simulations. At these small atmospheric perturbation levels, the response of the airglow is linear, as shown in

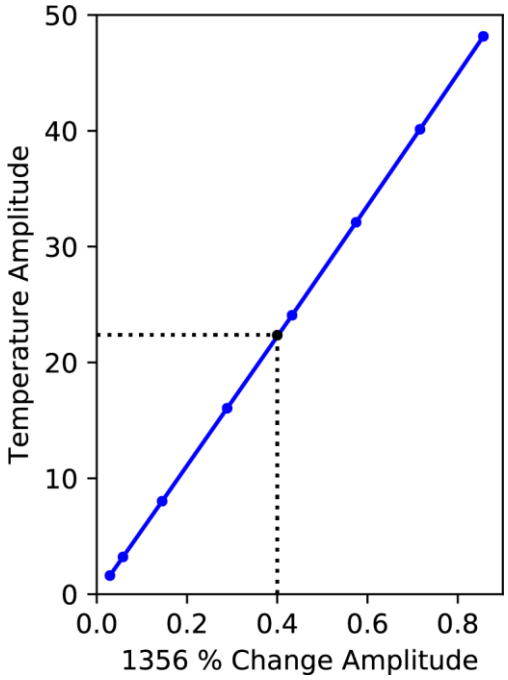

Figure *8*. The ~0.4% amplitude of the oxygen airglow perturbation noted in the previous section is consistent with an atmospheric temperature perturbation of around 22.4 K. To compare this with the observed disk temperatures, it is necessary to acknowledge that the amplitude of any realistic gravity wave perturbation will vary with altitude, and the 22.4 K value reported here refers to the perturbation at 150 km altitude, close to the peak of where the disk far-UV airglow originates. This is illustrated in more detail in Figure 9, which reproduces the atmospheric perturbations used and the airglow perturbation from GLOW that results. The variation in the wave amplitude and phase with altitude matches that used in Greer *et al*., [2018]. The amplitude of the temperature perturbation varies from around 12 K near 130 km to almost 36 K near 175 km. Similarly, the corresponding neutral density perturbation varies across this region, and has a value of 2.15 % at 150 km altitude.

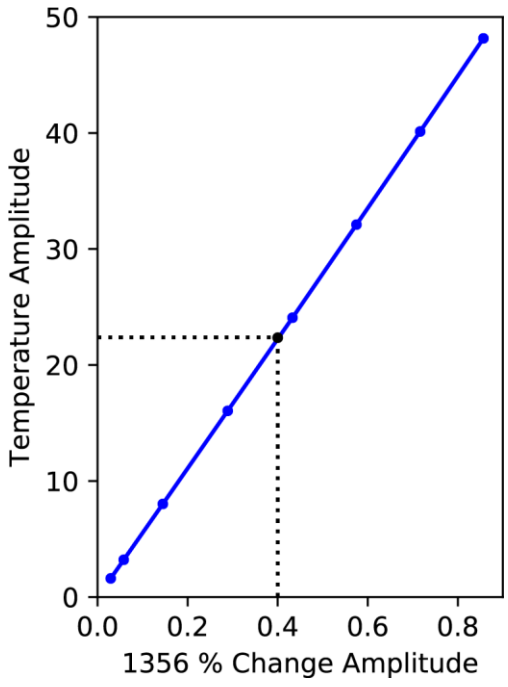

Figure 8 Results of the GLOW airglow simulations of the O 135.6 nm doublet at 45° north and 80° west for the geophysical conditions on October 18, 2019. The amplitude of the simulated airglow perturbation is shown as a function of the change in the neutral atmosphere, expressed in terms of the temperature. Simulations correspond to an average over 12 – 20 UT. The solid lines show the linear least-squares fit to these data.

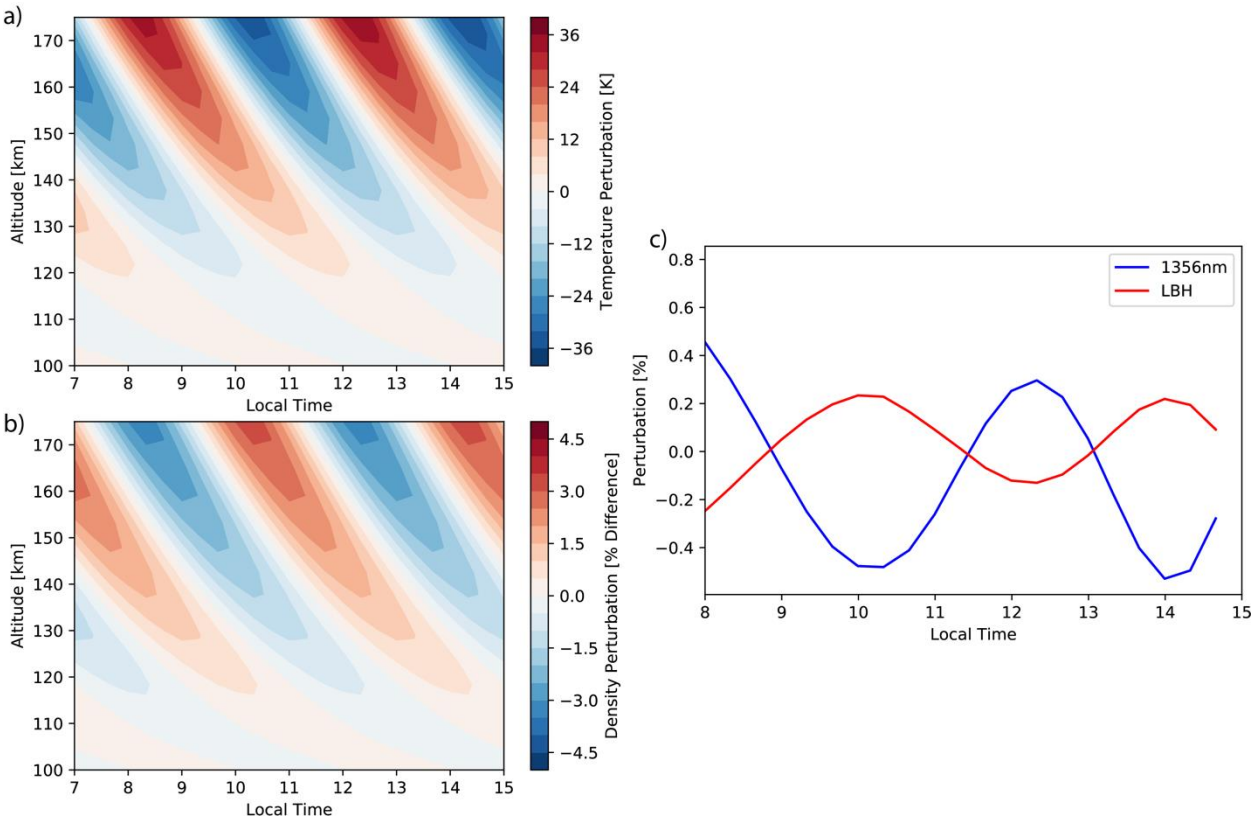

Figure 9 Impacts of the best-match gravity wave-like perturbation on the oxygen and nitrogen airglow brightness. Panel a shows the perturbation in temperature and panel b shows the perturbation in neutral density. Panel c shows the resultant impact of the wave-like perturbation from panels a and b on the oxygen and nitrogen airglow simulated using the GLOW model at 45° latitude and -80° longitude for the geophysical conditions on October 18. Note the variation in the amplitude of the atmospheric perturbation with altitude.

Examining Figure 9 in more detail, we see the phase offset between the oxygen airglow brightness and temperature perturbations, that match what is seen in the GOLD observations. The resultant oxygen and nitrogen airglow brightness perturbations reflect the antiphase relationship seen by GOLD. The disk temperature perturbation observed by GOLD was 13 K, which is similar to the simulated variation near 130 km, and is generally less than that in the best-fit simulation, shown in Figure 9. However, it is worth noting that the GOLD observation represents an altitude-integral of the temperature perturbation, weighted by the LBH airglow emission profile that peaks near 150 km, but extends over several 10s km above and below this altitude. Given this, and the tilted phase-fronts of any realistic gravity wave, the temperature perturbation seen by GOLD is expected to be less than the simulated value at the peak of the layer near 150 km. Without knowledge of the vertical wavelength of the wave observed at this time, it is not possible to provide a more quantitative relationship between the observed temperature perturbation and that simulated at any one altitude, other than to note they are generally consistent in this case. Taking all of these factors into consideration, we see that a gravity-wave similar to that shown in Figure 9 is consistent with all of the GOLD observed features.

4. Discussion and Conclusions

Results from a three-day campaign with the GOLD instrument to observe atmospheric waves in the atmosphere during October 2019 are presented. In the operating mode used for this campaign, GOLD obtained data during daytime by using one channel in a fixed viewing

direction, maximizing the signal and providing information along a line that is approximately aligned the meridional direction. To provide overlap with ground-based data, while being near nadir viewing geometry, GOLD Channel B was positioned over the eastern coast of the US. There, ground-based GPS TEC data are then available to help identify wave perturbations in ionospheric parameters, providing supporting information for the GOLD observations.

Perturbations are seen in the differential TEC data that are indicative of TIDs. As indicated in prior studies, wave-like TIDs are ubiquitous in GNSS dTEC datasets, and the three days of this campaign are no exception. Given how clearly such features are seen in the dTEC we use these data to determine the phase propagation of the waves on each of the three days. On October 18th, presented in detail, the waves appear to move ~7°/hour and are headed almost due south, with a horizontal wavelength of ~1500 km and a phase speed of 210 ms^{-1}. These properties are indicative of a slow-moving large-scale TID, consistent with the relatively low levels of geomagnetic activity present on this day. While determining the wave source is beyond the datasets at hand, the phase propagation direction is consistent with a source near the auroral region, but a lower-atmospheric source or secondary gravity wave source at intermediate altitude remain other possibilities. Additionally, the meridional speed of ~7°/hour and the time at which the features are see at mid-latitudes does not appear to line up with any pronounced auroral electrojet features (Figure 3), indicating that there is no obvious source of these waves.

GOLD sees similar wave-like perturbations in the airglow brightness associated with oxygen and nitrogen species, column O/N_2 ratio derived from those brightnesses and disk temperatures derived from the shape of the nitrogen LBH band. Using the phase propagation rates determined

for the dTEC signature, we demonstrate that these are moving at approximately the same rate, but the dTEC and GOLD oxygen signatures at not quite in phase with one another.

The phase and amplitude relationships between each quantity are examined by taking an average of the values over 20 – 50° latitude, after all have been adjusted using the phase propagation rates determined from dTEC. The oxygen and nitrogen airglow brightness perturbations are in antiphase with one another, producing a clear variation in the column O/N_2 ratio that is consistent with a response to vertical advection. The temperature perturbations appear shifted relative to the oxygen airglow by around one quarter wave period, with the temperature perturbations lagging or appearing slightly northwards of those in the LBH, consistent with an atmospheric gravity wave propagating southwards (and thus consistent with the original picture from the dTEC). The correspondence in the phase between the airglow and dTEC is only partial, but on two out of the three days the perturbations in dTEC appear to be mostly in phase with those in the oxygen airglow. Less correspondence in the amplitudes of the signals seen in dTEC and the airglow are seen (as measured by the changes in the R^2 values reported in Section 3.5), suggesting a complex relationship between the amplitude of these signals, even though both appear to be related in the measures described above. While the source of this complex relationship is unclear from these observations alone, one possibility is that the airglow signatures observed by GOLD and the TEC observations from the ground both represent altitude-averaged quantities with only limited overlap in altitude. The far UV airglow features GOLD observes are emitted over a range of altitudes and are strongest in the 130 – 180 km region, representative of the middle thermosphere. The TEC values are also an altitude integrated quantity and are most highly weighted to F-region altitudes, typically in the 250 – 350 km

662 region, which overlaps with the upper thermosphere. Neither GOLD nor the ground-based TEC
663 provide precise constraints on these altitude ranges, but it is reasonable to expect that any
664 changes in the wave properties (such as change in amplitude) with altitude could account for a
665 difference in the phase or amplitude seen in these two datasets. Additionally, the analysis
666 presented here focuses on only the strongest wave perturbations seen in the dTEC data and
667 identifies features moving at the same latitudinal rate as these. Any other waves or propagating
668 features present could be categorized as noise in this analysis and contribute to an apparent lack
669 of agreement. A final consideration is that perturbations in the F-region electron density may
670 tend to be aligned with the geomagnetic field, whereas the neutral perturbations are not. The
671 interplay of this, and the measure of TEC, which is a vertical column will likely vary between
672 the higher latitudes where the field is aligned nearly vertically and lower latitudes where it is not.
673 This may provide another source of discrepancy between the dTEC perturbations and those
674 observed in the neutral atmosphere with GOLD.
675
676 Using the GLOW airglow model, we demonstrated the consistency of the signatures observed by
677 GOLD with a gravity wave perturbation to the atmosphere. The model, with a background
678 atmosphere that is perturbed by a gravity-wave like structure is able to reproduce fluctuations in
679 the airglow brightness that have the same kind of phase-relationship as that observed. The best-
680 fit amplitude of the atmospheric perturbation is 22.4 K temperature and 2.15 % density variation
681 at 150 km. Given the altitude range of the airglow emission, the tilt in any phase of the
682 perturbation (corresponding to an unknown vertical wavelength), and the growth in the
683 amplitude of a perturbation with height, the observed disk temperature perturbation is expected
684 to be smaller than that simulated at the 150 km altitude, which is the case. The phase between the

685 density, temperature and airglow perturbations are all consistent with the simulated gravity
686 wave-like feature.
687
688 This campaign yields a number of important findings. First is that the GOLD disk temperature
689 data show the signatures of the TADs very clearly – arguably better than the airglow brightness
690 data used in a prior study. This is of particular interest as observations of the temperature in the
691 middle thermosphere are extremely sparse, and thus estimates of the amplitude of wave
692 perturbations of these temperatures are similarly rare. Second is that the phase relationships
693 between the observed perturbations in the oxygen and nitrogen airglow, the column O/N_2 and the
694 disk temperatures are all consistent with the perturbations coming from an atmospheric gravity
695 wave or TAD. Third is that the TAD and TID seen in the dTEC data propagate at the same rate
696 but have a complex relationship between their amplitudes that is not easy to determine from just
697 a sample of 3 days. With these findings in mind, as GOLD moves into its extended mission
698 (beginning November 2020), campaigns such as that described here will be performed more
699 frequently. Lessons learned from this campaign and the methods described here will allow a
700 much larger dataset of TAD and TID pairs to be identified, under different conditions and for
701 different seasons, with the hope that the relationship between these two can be characterized.
702
703 **Acknowledgements**

704 This research was supported by NASA contract 80GSFC18C0061. The GOLD data are available
705 from the GOLD Science Data Center (http://gold.cs.ucf.edu/search/) and NASA's Space Physics
706 Data Facility (https://spdf.gsfc.nasa.gov). GPS TEC data products and access through the
707 Madrigal distributed data system are provided to the community (http://www.openmadrigal.org)

by the Massachusetts Institute of Technology (MIT) under support from the U.S. National Science Foundation (NSF) Grant AGS- AGS-195273. SRZ also acknowledges AFOSR MURI Grant FA9559-16-1-0364. The F10.7 data are available from NASA's OMNIWeb (https://omniweb.gsfc.nasa.gov). The SME Auroral Electrojet Index data are available from the SuperMAG at http://supermag.jhuapl.edu and we gratefully acknowledge the SuperMAG collaborators.

References

Andrews, D.G., Holton, J.R., Leovy, C.B., 1987. Middle atmosphere dynamics, International geophysics series. Academic Press, Orlando.

Aksnes, A., R. Eastes, S. Budzien, K. Dymond, Neutral temperatures in the lower thermosphere from N_2 Lyman-Birge-Hopfield (LBH) band profiles. Geophys. Res. Lett. **33**, L15103 (2006). doi:10.1029/ 2006GL026255

Azeem, I., Vadas, S. L., Crowley, G., & Makela, J. J. (2017). Traveling ionospheric disturbances over the United States induced by gravity waves from the 2011 Tohoku tsunami and comparison with gravity wave dissipative theory. Journal of Geophysical Research: Space Physics, 122, 3430–3447. https://doi.org/10.1002/2016JA023659

Bilitza, D. (2018). IRI the international standard for the ionosphere. Advances in Radio Science, 16, 1–11. https://doi.org/10.5194/ ars-16-1-2018

727 Bruinsma, S., Forbes, J. M., Nerem, R. S., & Zhang, X. (2006). Thermosphere density response
728 to the 20–21 November 2003 solar and geomagnetic storm from CHAMP and GRACE
729 accelerometer data. Journal of Geophysical Research, 111, A06303. https://doi.org/
730 10.1029/2005JA011284

731 Bruinsma, S. L., & Forbes, J. M. (2008). Medium- to large-scale density variability as observed
732 by CHAMP. Space Weather, 6, S08002. https://doi.org/10.1029/2008SW000411

733 Djuth, F. T., Zhang, L. D., Livneh, D. J., Seker, I., Smith, S. M., Sulzer, M. P., et al. (2010).
734 Arecibo's thermospheric gravity waves and the case for an ocean source. Journal of Geophysical
735 Research, 115, A08305. https://doi.org/10.1029/2009JA014799

736 Earle, G. D., Musumba, A. M., & Vadas, S. L. (2008). Satellite-based measurements of gravity
737 wave-induced midlatitude plasma density perturbations. Journal of Geophysical Research, 113,
738 A03303. https://doi.org/10.1029/2007JA012766

739 Eastes, R. W., McClintock, W. E., Burns, A. G., Anderson, D. N., Andersson, L., Codrescu, M.,
740 et al. (2017). The Global-Scale Observations of the Limb and Disk (GOLD) mission. Space
741 Science Reviews, 212(1-2), 383–408. https://doi.org/10.1007/s11214-017-0392-2

742 Eastes, R. W., Solomon, S. C., Daniell, R. E., Anderson, D. N., Burns, A. G., England, S. L., et
743 al. (2019). Global-scale observations of the equatorial ionization anomaly. Geophysical Research
744 Letters, 46(16), 9318–9326. https://doi.org/10.1029/2019GL084199

745 England, S. L., Greer, K. R., Solomon, S. C., Eastes, R. W., McClintock, W. E., & Burns, A. G.
746 (2020). Observation of thermospheric gravity waves in the Southern Hemisphere with GOLD.

747 Journal of Geophysical Research: Space Physics, 125, e2019JA027405. https://
748 doi.org/10.1029/2019JA027405

749 Galushko, V.G., Paznukhov, V.V., Yampolski, Y.M. *et al.* Incoherent scatter radar observations
750 of AGW/TID events generated by the moving solar terminator. *Annales Geophysicae* 16**,** 821–
751 827 (1998). https://doi.org/10.1007/s00585-998-0821-3

752 Garcia, R. F., Bruinsma, S., Massarweh, L., & Doornbos, E. (2016). Medium-scale gravity wave
753 activity in the thermosphere inferred from GOCE data. Journal of Geophysical Research: Space
754 Physics, 121, 8089–8102. https://doi.org/10.1002/2016JA022797

755 Gjerloev, J. W. (2012), The SuperMAG data processing technique, J. Geophys. Res., 117,
756 A09213, doi:10.1029/2012JA017683.

757 Greer, K. R., England, S. L., Becker, E., Rusch, D., & Eastes, R. (2018). Modeled gravity wave-
758 like perturbations in the brightness of far ultraviolet emissions for the GOLD mission. Journal of
759 Geophysical Research: Space Physics, 123, 5821–5830. https://doi.org/10.1029/ 2018JA025501

760 Livneh, D. J., I. Seker, F. T. Djuth, and J. D. Mathews (2009), Omnipresent vertically coherent
761 fluctuations in the ionosphere with a possible worldwide-midlatitude extent, J. Geophys. Res.,
762 114, A06303, doi:10.1029/2008JA013999.

763 Mandal, S., and Pallamraju, D., (2020), Thermospheric gravity wave characteristics in the
764 daytime over low-latitude during geomagnetically quiet and disturbed conditions, J. Atmos. Sol.-
765 Terr. Phys., 211, https://doi.org/10.1016/j.jastp.2020.105470

766 McClintock, W. E., Solomon, S. C., Eastes, R., Anderson, D. N., Andersson, L., Burns, A. G., et
767 al. (2017), Global-scale Observations of the Limb and Disk (GOLD): Science implementation.
768 American Geophysical Uniton Fall Meeting, SA31A-2561.

769 Melèndez-Alvira, D. J., Meier, R. R., Picone, J. M., Feldman, P. D., & McLaughlin, B. M.
770 (1999). Analysis of the oxygen nightglow measured by the Hopkins Ultraviolet Telescope:
771 Implications for ionospheric partial radiative recombination rate coefficients. Journal of
772 Geophysical Research, 104(A7), 14,901–14,913. https://doi.org/10.1029/1999JA900136

773 Negrea, C., Zabotin, N., Bullett, T., Fuller-Rowell, T., Fang, T.-W., & Codrescu, M. (2016).
774 Characteristics of acoustic gravity waves obtained from Dynasonde data. Journal of Geophysical
775 Research: Space Physics, 121, 3665–3680. https://doi.org/10.1002/2016JA022495

776 Newell, P. T., and J. W. Gjerloev (2011), Evaluation of SuperMAG auroral electrojet indices as
777 indicators of substorms and auroral power, J. Geophys. Res., 116, A12211,
778 doi:10.1029/2011JA016779.

779 Park, J., Lühr, H., Lee, C., Kim, Y. H., Jee, G., & Kim, J.-H. (2014). A climatology of medium-
780 scale gravity wave activity in the midlatitude/low-latitude daytime upper thermosphere as
781 observed by CHAMP. Journal of Geophysical Research: Space Physics, 119, 2187–2196.
782 https://doi.org/10.1002/2013JA019705

783 Paulino, I., Moraes, J. F., Maranhão, G. K., Wrasse, C. M., Buriti, R. A., Medeiros, A. F., et al.
784 (2018). Intrinsic parameters of periodic waves observed in the OI6300 airglow layer over the
785 Brazilian equatorial region. Annales de Geophysique, 36, 265–273. https://doi.org/10.5194/
786 angeo-36-265-2018

Richmond, A. D. (1978). Gravity wave generation, propagation, and dissipation in the thermosphere. Journal of Geophysical Research, 83(A9), 4131–4145. https://doi.org/10.1029/JA083iA09p04131

Rideout, W., & Coster, A. (2006). Automated GPS processing for global total electron content data. *GPS Solutions*, *10*, 219–228. https://doi.org/10.1007/s10291- 006- 0029- 5

Savitzky, A., & Golay, M. J. E. (1964). Smoothing and differentiation of data by simplified least squares procedures. *Analytical Chemistry*, *36*, 1627–1639

Shiokawa, K., Lu, G., Otsuka, Y., Ogawa, T., Yamamoto, M., Nishitani, N., and Sato, N. (2007), Ground observation and AMIE-TIEGCM modeling of a storm-time traveling ionospheric disturbance, *J. Geophys. Res.*, 112, A05308, doi:10.1029/2006JA011772.

Solomon, S. C. (2017). Global modeling of thermospheric airglow in the far ultraviolet. Journal of Geophysical Research: Space Physics, 122, 7834–7848. https://doi.org/10.1002/2017JA024314

Strickland, D. J., J. S. Evans, and L. J. Paxton (1995), Satellite remote sensing of thermospheric O/N_2 and solar EUV, 1, Theory, *J. Geophys. Res.*, *100*, 12,217.

Tsuchiya, S., Shiokawa, K., Otsuka, Y., Nakamura, T., Yamamoto, M., Connors, M., et al. (2020). Wavenumber spectra of atmospheric gravity waves and medium-scale traveling ionospheric disturbances based on more than 10-year airglow images in Japan, Russia, and Canada. *Journal of Geophysical Research: Space Physics*, 125, e2019JA026807. https://doi.org/10.1029/2019JA026807

807 Tsugawa, T., Y. Otsuka, A. J. Coster, and A. Saito (2007), Medium-scale traveling ionospheric
808 disturbances detected with dense and wide TEC maps over North America, Geophys. Res. Lett.,
809 34, L22101, doi:10.1029/2007GL031663

810 Vadas, S. L., & Fritts, D. C. (2006). Influence of solar variability on gravity wave structure and
811 dissipation in the thermosphere from tropospheric convection. Journal of Geophysical Research,
812 111, A10S12. https://doi.org/10.1029/2005JA011510

813 Vadas, S. L., & Liu, H.-L. (2009). The generation of large-scale gravity waves and neutral winds
814 in the thermosphere from the dissipation of convectively-generated gravity waves. Journal of
815 Geophysical Research, 114, A10310. https://doi.org/10.1029/2009JA014108

816 Vierinen, J., Coster, A. J., Rideout, W. C., Erickson, P. J., & Norberg, J. (2016). Statistical
817 framework for estimating GNSS bias. *Atmospheric Measurement Techniques*, *9*, 1303–1312.
818 https://doi.org/10.5194/amt-9-1303-2016

819 Yiğit, E., & Medvedev, A. S. (2015). Internal wave coupling processes in Earth's atmosphere.
820 Advances in Space Research, 55(4), 983–1003. https://doi.org/10.1016/j.asr.2014.11.020

821 Yiğit, E., Medvedev, A. S., England, S. L., & Immel, T. J. (2014). Simulated variability of the
822 high-latitude thermosphere induced by small-scale gravity waves during a sudden stratospheric
823 warming. Journal of Geophysical Research: Space Physics, 119, 357–365. https://
824 doi.org/10.1002/2013JA019283

825 Zhang, S.-R., Coster, A. J., Erickson, P. J., Goncharenko, L. P., Rideout, W., & Vierinen, J.
826 (2019). Traveling ionospheric disturbances and ionospheric perturbations associated with solar

flares in September 2017. *Journal of Geophysical Research: Space Physics*, *124*, 5894–5917. https://doi.org/10. 1029/2019JA026585

Zhang, Y., Paxton, L.J., Morrison, D., and Schaefer, B. (2018). Storm-time variations of atomic nitrogen 149.3 nm emission. *J. Atmos. Sol.-Terr. Phys.*, 169, 78-82. https://doi.org/10.1016/j.jastp.2018.01.023.

Zhang, Y., L. J. Paxton, D. Morrison, B. Wolven, H. Kil, C.-I. Meng, S. B. Mende, and T. J. Immel (2004), O/N_2 changes during 1–4 October 2002 storms: IMAGE SI-13 and TIMED/GUVI observations, J. Geophys. Res., 109, A10308, doi:10.1029/2004JA010441.

Figure 10 Location of the GOLD Channel B observations during the campaign. A purple plus symbol marks the location of each of the 376 data bins along the length of the image. The light blue dots show the locations of the GPS dTEC data included in this study.

Figure 11 Global Navigation Satellite System differential TEC (dTEC) for October 18, 2019 as functions of latitude and universal time. The range of longitudes included is indicated in panels a through c. The overlaid black lines in panel b mark locations of local maxima used to find the approximate latitudinal phase velocity of the features seen, as described in the text.

Figure 12 One-minute SME Auroral Electrojet Index for the 3 days of the campaign during October 2019. The time-periods corresponding to the GOLD observations are highlighted with the yellow shaded regions.

Figure 13 Example spectrum made from summing 100 Level 1b exposures from the GOLD data from October 18, 2019. The light blue symbols highlight the region used to identify the atomic oxygen feature and the dark blue highlight the corresponding background area. The yellow symbols highlight the region used to identify the nitrogen features and the dark purple highlight the corresponding background area.

Figure 14 Perturbations to the airglow, composition and temperature observed on October 18, 2019. Panel a shows the perturbation in the oxygen airglow. Panel b shows the perturbation in the nitrogen airglow. Panel c shows the perturbation in the oxygen minus twice the nitrogen airglow to highlight the difference. Panel d shows the oxygen airglow minus twice the nitrogen airglow, where the universal times at each latitude have been offset to correspond to the time at

47° latitude, using the latitudinal phase propagation rates derived from the dTEC data, as described in the text. Panels e and f are as c and d, but for the column O/N_2 perturbations derived from the oxygen and nitrogen airglow brightnesses. Panels f and h are as c and d, but for the perturbations in the disk temperature derived from the shape of the LBH band emission.

Figure 15 Panels a through d show the mean perturbation in the 135.6 nm airglow compared to the LBH airglow, column O/N_2, disk temperatures, and dTEC perturbations respectively. All data are averaged over 20 – 50° latitude, and are shifted in UT to a common value at 47° north as in Figure 5. Panels a through d correspond to the results for October 17, 2019. Panels e through h show the same as a through d, but for October 18, 2019. Panels i through l show the same as a through d, but for October 19, 2019. In each panel, the red line corresponds to the oxygen airglow. The airglow values are in counts. The disk temperatures are in K and are multipled by 0.2 to be visible on this scale. The column O/N_2 are dimensionless ratios and are multipled by 200 to be visible on this scale. The dTEC values are in TECu and are multiplied by 20 to be visible on this scale.

Figure 16 Correlations between the perturbations in the oxygen and nitrogren airglow brightness, disk temperatures, column O/N_2 and dTEC for October 18 2019 data shown in Figure 6. Panel a shows the nitrogen airglow brightness vs the oxygen airglow brightness. Panel b shows the O/N_2 ratio vs the nitrogen airglow brightness. Panel c shows the nitrogen airglow brightness vs the disk temperature. Panel d shows the dTEC vs the oxygen airglow brightness. All datasets have been interpolated onto a 10-minute cadence, and the temperature data were shifted by 1 hour, corresponding to approximately one quarter wave period. The pink lines show

the least-squares linear fits to each pair of data. Coefficients of determination for each of these linear fits are shown.

Figure 17 Results of the GLOW airglow simulations of the O 135.6 nm doublet at 45° north and 80° west for the geophysical conditions on October 18, 2019. The amplitude of the simulated airglow perturbation is shown as a function of the change in the neutral atmosphere, expressed in terms of the temperature. Simulations correspond to an average over 12 – 20 UT. The solid lines show the linear least-squares fit to these data.

Figure 18 Impacts of the best-match gravity wave-like perturbation on the oxygen and nitrogen airglow brightness. Panel a shows the perturbation in temperature and panel b shows the perturbation in neutral density. Panel c shows the resultant impact of the wave-like perturbation from panels a and b on the oxygen and nitrogen airglow simulated using the GLOW model at 45° latitude and -80° longitude for the geophysical conditions on October 18. Note the variation in the amplitude of the atmospheric perturbation with altitude.

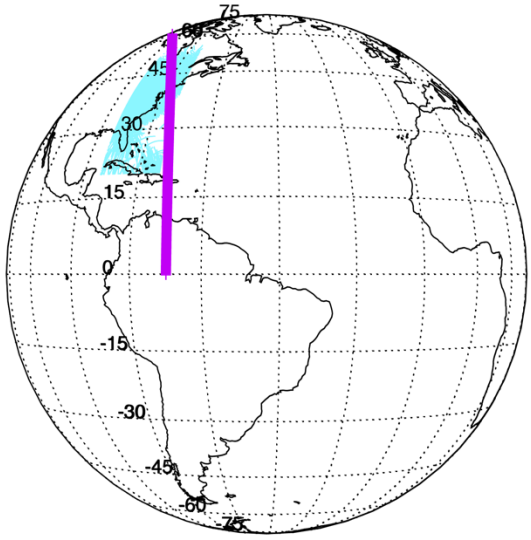
75
60
45
30
15
0
-15
-30
-45
-60
-75

900

901

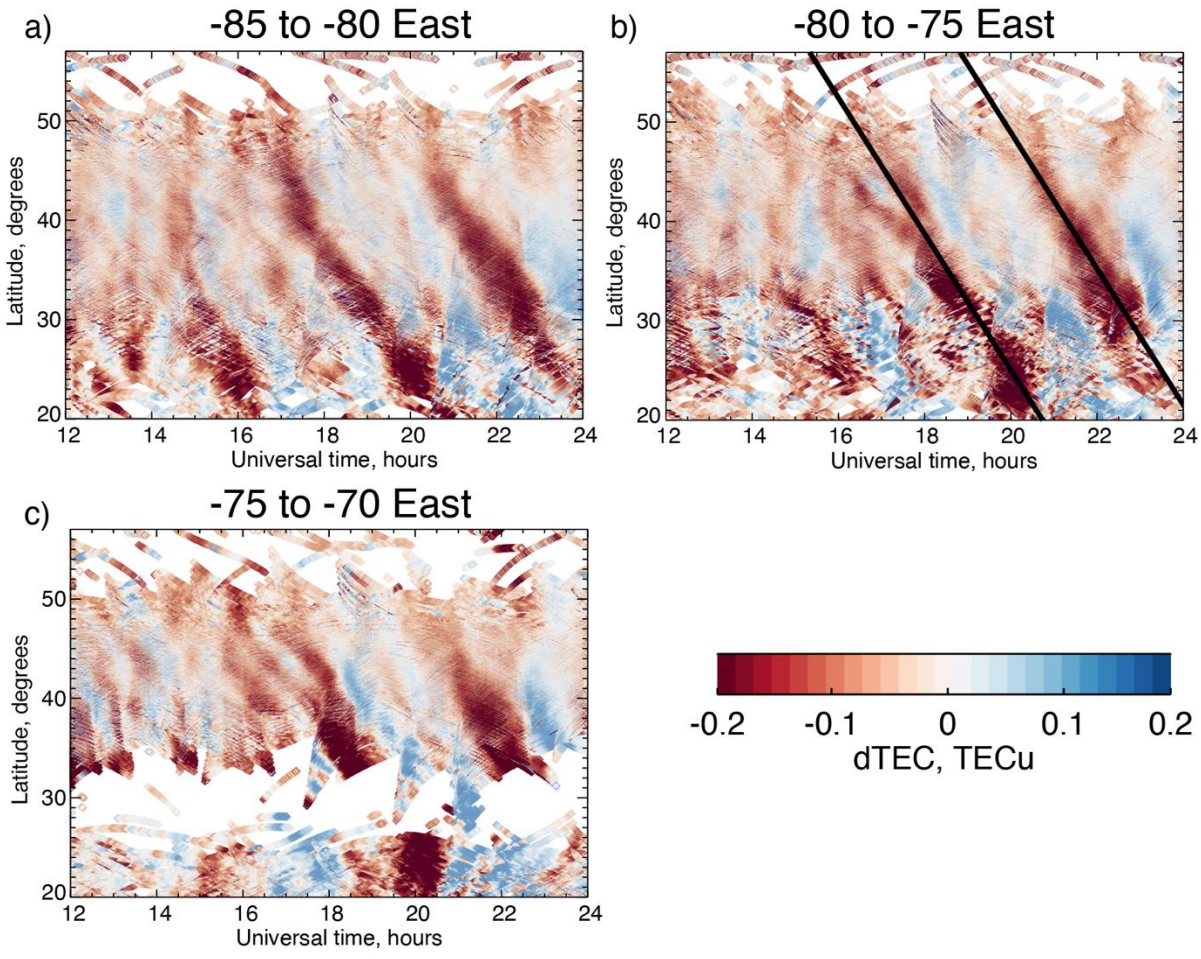
a)
-85 to -80 East
b)
-80 to -75 East
c)
-75 to -70 East
Latitude, degrees
Universal time, hours
20
30
40
50
12
14
16
18
20
22
24
-0.2
-0.1
0
0.1
0.2
dTEC, TECu

902

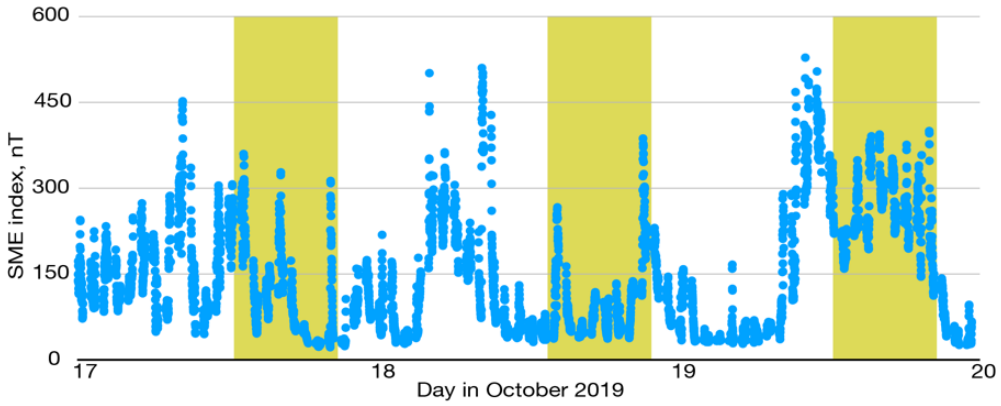

903

904

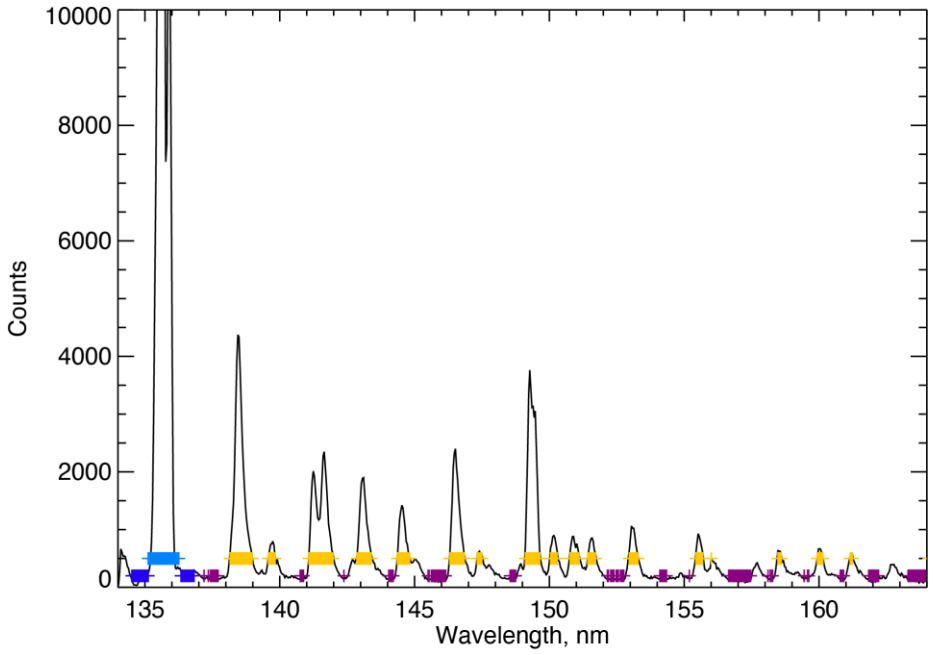

905

906

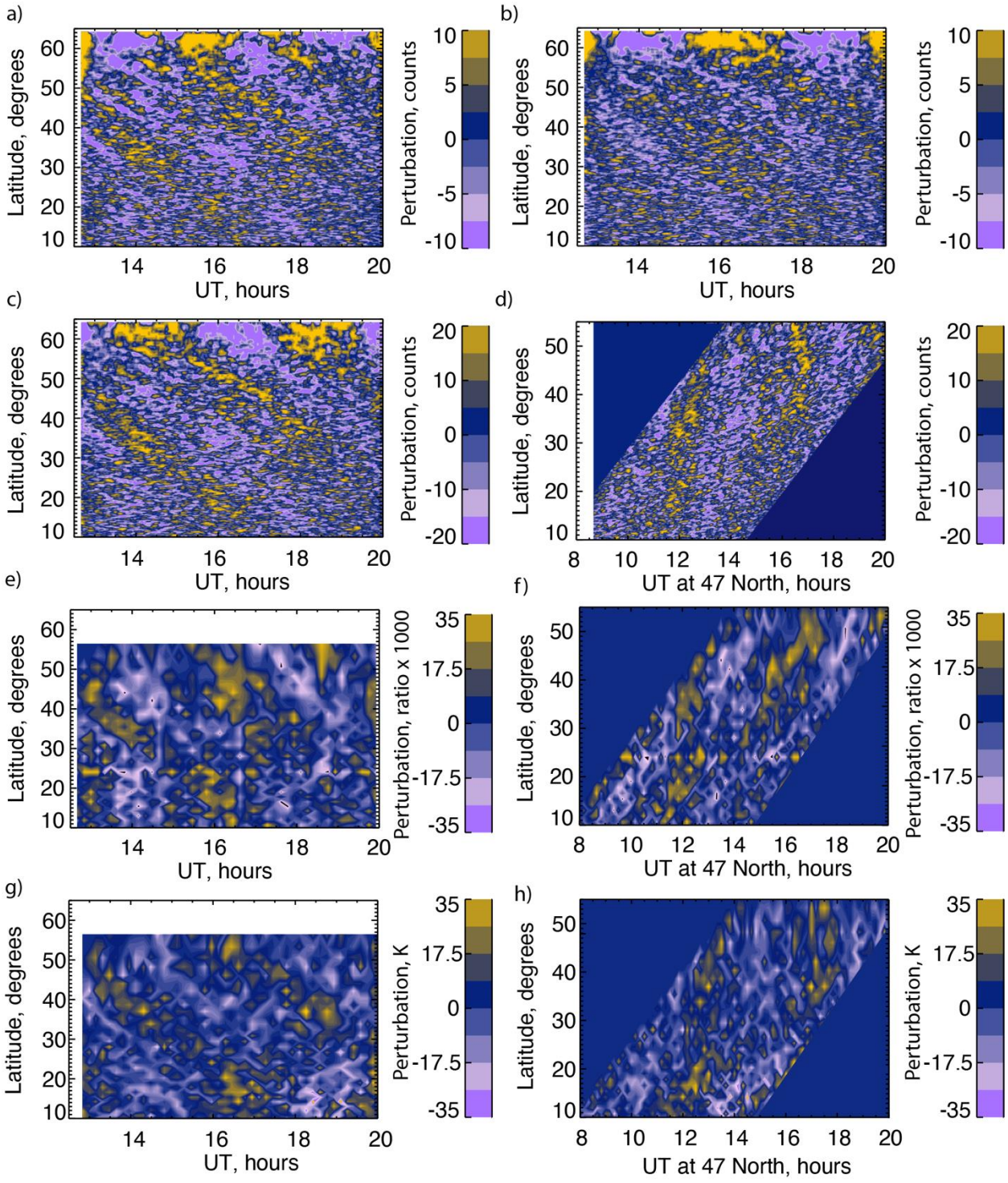
a)
b)
c)
d)
e)
f)
g)
h)
Latitude, degrees
UT, hours
UT at 47 North, hours
Perturbation, counts
Perturbation, ratio x 1000
Perturbation, K

907

908

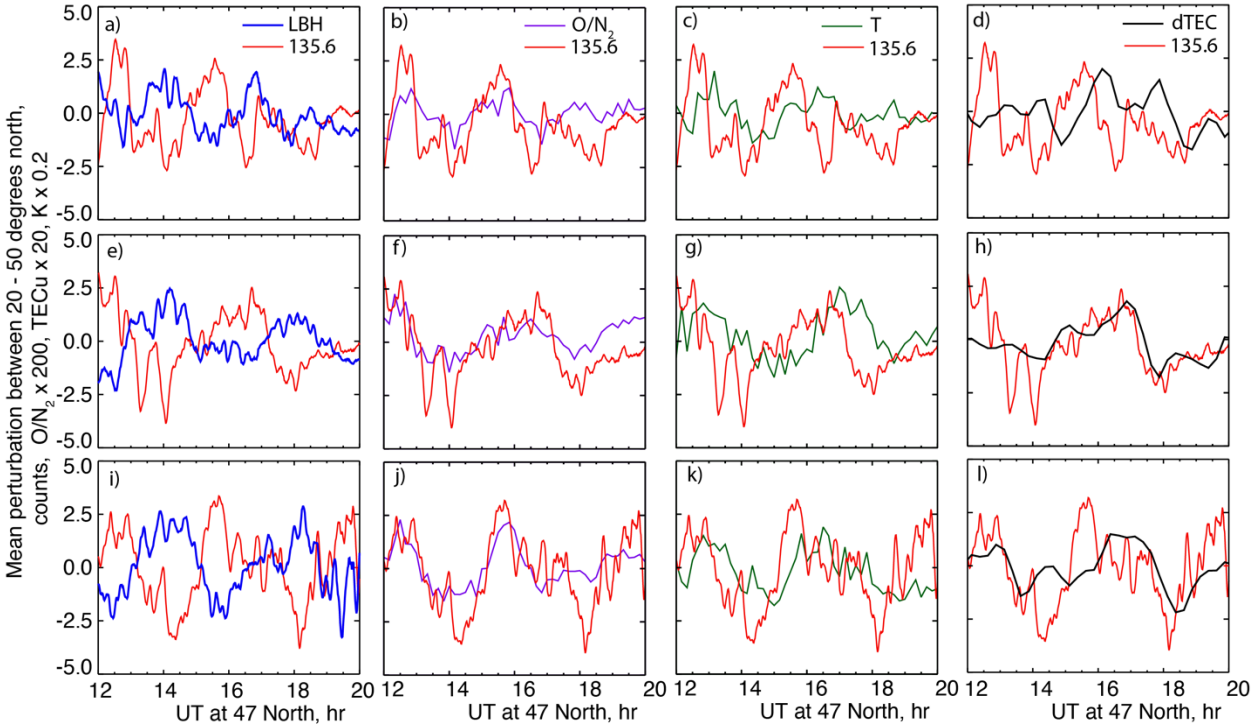

909

910

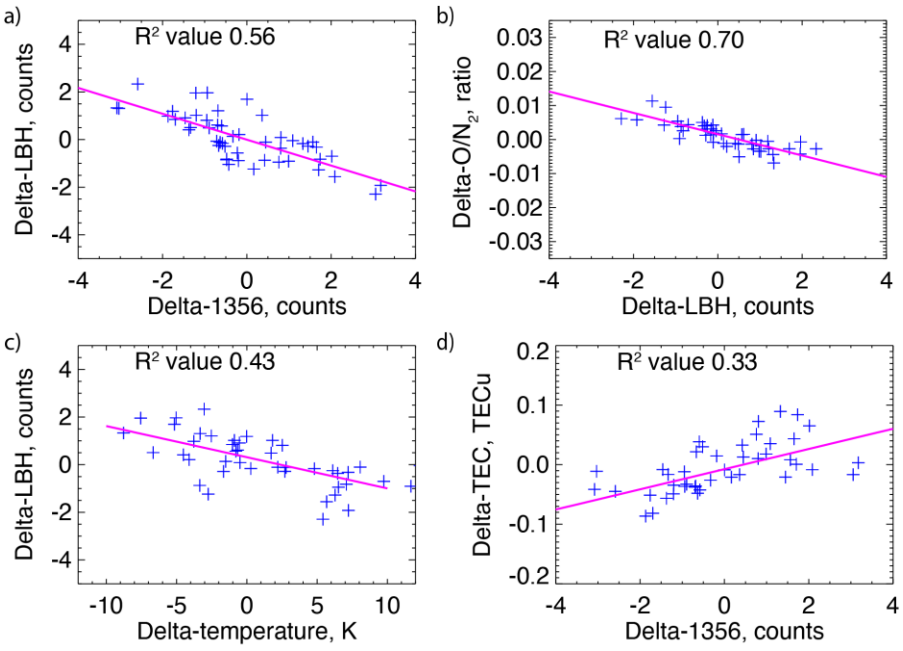

911

912

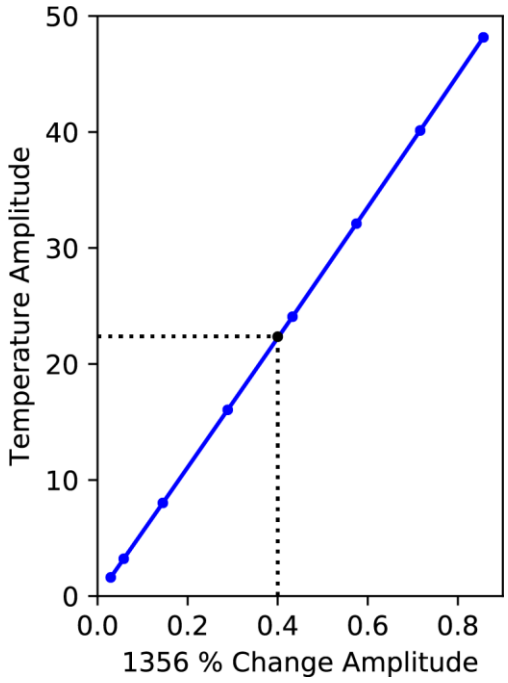
Temperature Amplitude
1356 % Change Amplitude
0
10
20
30
40
50
0.0
0.2
0.4
0.6
0.8

913

914

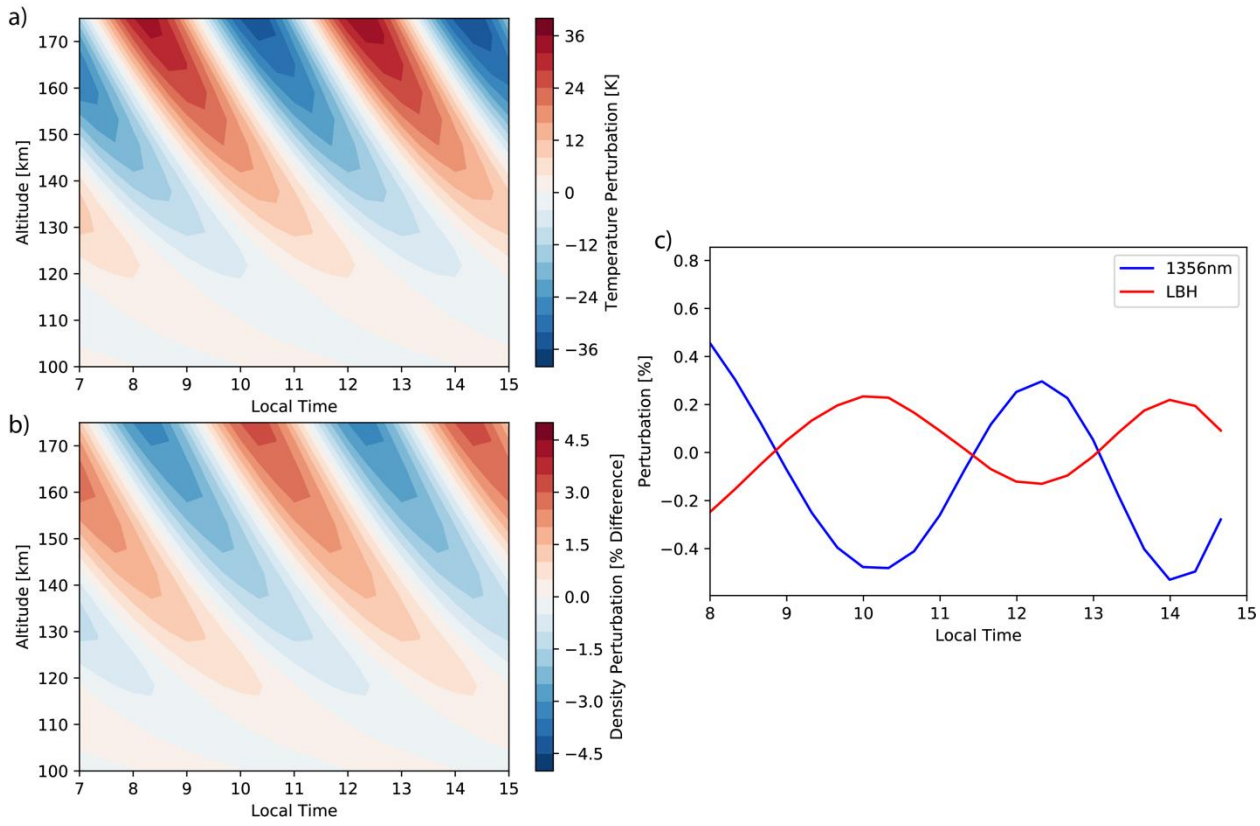
a)
b)
c)
Altitude [km]
Local Time
Temperature Perturbation [K]
Density Perturbation [% Difference]
Perturbation [%]
1356nm
LBH

915